Numerical investigations of two-phase finger-like instabilities

Alexandre Chiapolino[1b], Richard Saurel[2a,b]

[a]*Aix Marseille Univ, CNRS, Centrale Marseille, LMA, Marseille, France*
[b]*RS2N, Chemin de Gaumin, Saint-Zacharie 83640, France*

Abstract

The aim of the present work is to progress in the identification of the effects responsible for the formation of jets in heterogeneous gas-particle cylindrical and spherical explosions. In this direction three two-phase flow models are considered, namely Baer and Nunziato's (BN) (1986) model, Marble's (1963) model and the dense-dilute model of Saurel et al. (2017). The first and third ones involve both non-conservative terms and viscous drag effects while the second one involves viscous drag only as interaction force. Computed results show that viscous drag alone is unable to reproduce finger-like instabilities. The BN model and the dense-dilute one differ significantly by their acoustic properties. It is shown that the only model able to reproduce qualitatively finger-like jets is the dense-dilute model. Mesh dependence of the results is studied as well as presence or absence of viscous drag. It appears that the non-conservative terms seem responsible for jetting effects.

Keywords: hyperbolic, particle jets, explosions

[1]`alexandre.chiapolino@rs2n.eu`
[2]`richard.saurel@rs2n.eu`

1. Introduction

When a spherical or cylindrical explosive charge is surrounded by a liquid layer or a granular particle bed, material dispersal occurs through particle jets having well-defined size. On the example shown in Fig. 1, a cylindrical explosive charge is initially surrounded by a liquid water layer.
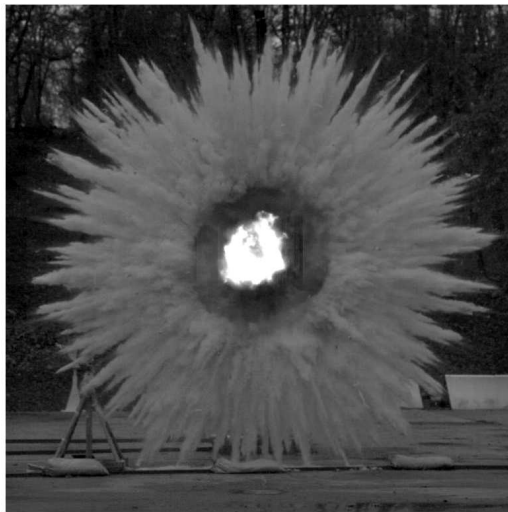

Figure 1: A cylindrical explosive charge is initially surrounded by a liquid layer. When the charge explodes the liquid layer transforms to a cloud of droplets forming highly dynamical particle jets. Same jetting effects appear when the liquid is replaced by a granular layer. These jets are present in cylindrical and spherical dispersal explosions.

Gas expansion during explosion fragments the liquid layer to a cloud of droplets that form highly dynamical particle jets. The same observation is reported when a granular bed is used instead of a liquid layer. Dispersion is consequently clearly multidimensional in the sense that one-dimensional (cylindrical or spherical) computations result in significant errors in predicting presence of materials.

With liquids, fragmentation occurs very fast, typically on time scales of a few microseconds, depending on the size of the liquid layer, in situations involving dispersion by explosives. The cloud of droplets becomes permeable very quickly and jets appear gradually. These jets are observed for any type of liquid layer, any powder, mono or polydisperse, in the presence or absence of water.

Experimental and numerical studies of this phenomenon have been carried out by Zhang et al. (2001) [1], Milne et al. (2010) [2], Frost (2010) [3], Parrish and Worland (2012) [4], Osnes et al. (2019) [5], Utkin (2019) [6] to cite a few. Simplified situations have been considered in Rodriguez et al. (2013) [7] and Xue et al. (2018) [8]. The explosive is replaced by a shock tube and the matter to disperse is placed between two plates, in a Hele-Shaw cell. Other simplified situations have been considered for example in McGrath et al. (2018) [9], Osnes et al. (2018) [10], Carmouze et al. (2018) [11] to study possible clustering effects due to aerodynamic forces. It seems that the formation of jets and the size selection mechanism are still unidentified.

In the present paper, a configuration like the one considered in Rodriguez et al. (2013) [7] with a Hele-Shaw cell and a particle ring is studied. Such Hele-Shaw cell configuration allows to omit 3D effects. The simulations of the present paper are indeed 2D for the sake of simplicity.

Typical results reported in Rodriguez's thesis [12] are shown in Fig. 2 at times 5 ms, 8 ms and 57 ms after rupture of the shock tube diaphragm, inducing shock wave and gas flow through a ring of flour particles. This configuration has been studied in Carmouze et al. (2019) [13] as well.
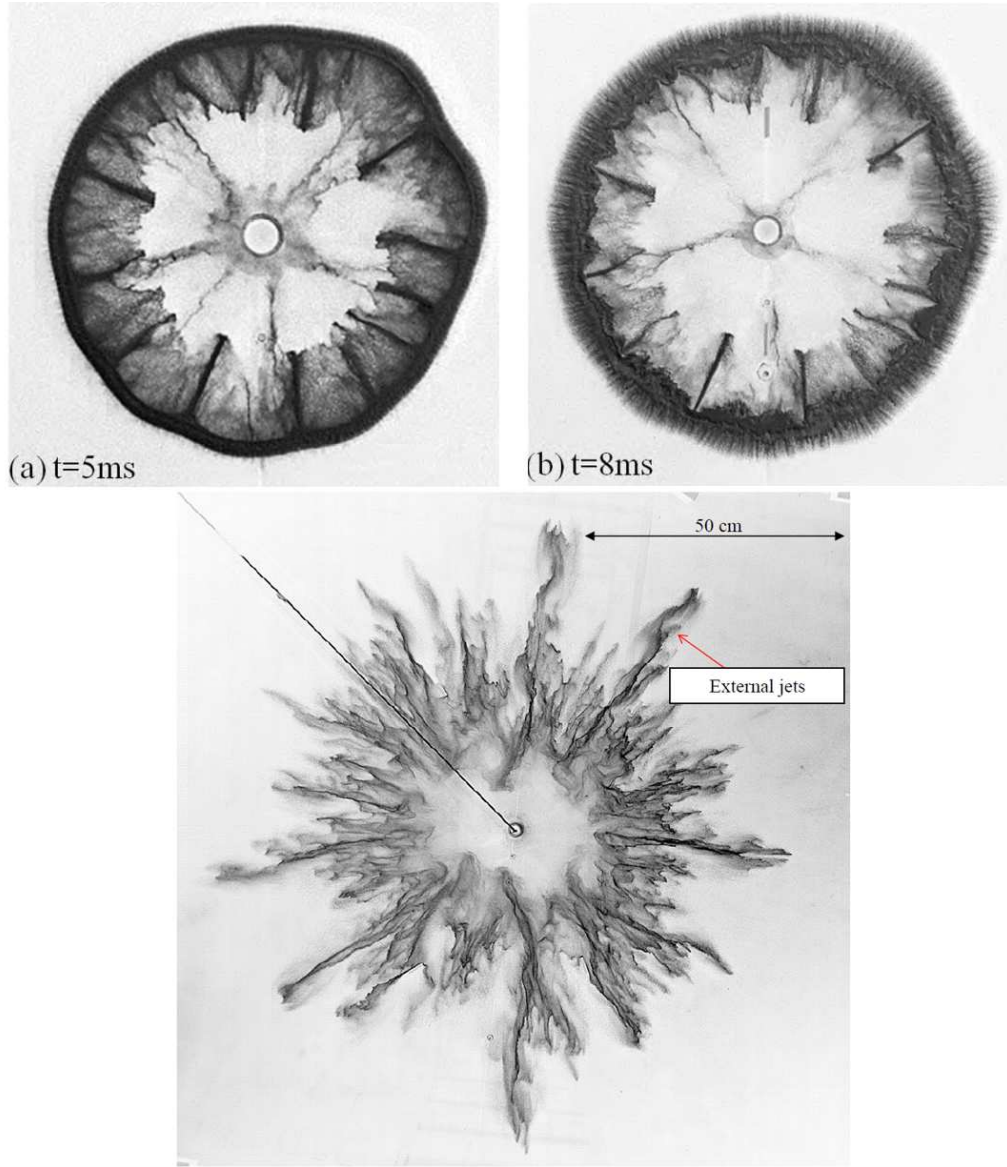
Figure 2: Typical interfacial instabilities reported in Rodriguez's thesis [12] and papers [7], as well as in Xue et al. (2018) [8]. Impulsive motion of a particle ring by a gas flow induces well defined particle fingers flowing to the center direction, oppositely to the gas flow. At later times, here at 8 ms, short wavelength instabilities also appear at the external surface. As time evolves, external surface instabilities grow and become dominant, as shown in the third picture at time 57 ms. Internal jets are thus observed at early times, followed by external ones at late times.

As reported by Rodriguez et al. (2013) [7] and Xue et al. (2018) [8], instabilities appear first at the inner interface and second at the outer one. Shape of these fingers is singular, in the sense that they do not qualitatively compare to Richtmyer-Meshkov instabilities or Rayleigh-Taylor ones, nor any other known instability. Indeed, mushroom-type shape is observed with these two

4

instabilities, while fingers are observed in the present context.

In the present paper, the origin of such finger-like instabilities is investigated with the help of numerical experiments. To the authors' knowledge, such instabilities have been successfully computed for the first time, at least qualitatively, in Carmouze et al. (2019) [13] with the help of the dense-dilute model of Saurel et al. (2017) [14].

In the present contribution, deeper investigation of the instability formation mechanism is achieved. Computed results are reported with the help of the three existing two-phase hyperbolic models. The first one is the non-equilibrium model of Saurel et al. (2003) [15], a variant of Baer and Nunziato's (BN) model (1986) [16]. The second one is the dilute model of Marble (1963) [17]. The third one is the dense-dilute model of Saurel et al. (2017) [14].

Comparing the computed results with these three different models is important to identify the effect responsible for the appearance of these particle jets. Indeed, with Marble's model (1963) [17] the only interaction effect is related to the viscous drag force. With the BN-type model [15] and the dense-dilute model [14] two types of interactions are present. The conventional (viscous) drag force, as in Marble's model, and a "differential drag force" due to the presence of non-conservative terms in the momentum and energy equations. As will be shown, differential drag appears as leading effect in the selection process of these jets. It is also shown that the BN-type model fails in the qualitative prediction of these particle jets, while the dense-dilute one predicts both inner and outer jets visible in the experiments reported in Fig. 2.

This paper is organized as follows. In Section 2 the BN-type model [15] and its properties are presented followed by Marble's model [17] and the dense-dilute model [14] in Sections 3 and 4 respectively. Viscous drag interaction effects are introduced in Section 5 and computed results are provided in Section 6. Conclusions are given in Section 7.

2. BN-type flow model

The total disequilibrium two-phase flow model was originally proposed by Baer and Nunziato
(1986) [16]. The balance equations for phases 1 and 2 are,

$$
\begin{cases}
\dfrac{\partial \alpha_1}{\partial t} + u_I \dfrac{\partial \alpha_1}{\partial x} = \mu(p_1 - p_2), \\[2mm]
\dfrac{\partial (\alpha_1 \rho_1)}{\partial t} + \dfrac{\partial (\alpha_1 \rho_1 u_1)}{\partial x} = 0, \\[2mm]
\dfrac{\partial (\alpha_1 \rho_1 u_1)}{\partial t} + \dfrac{\partial (\alpha_1 (\rho_1 u_1^2 + p_1))}{\partial x} = p_I \dfrac{\partial \alpha_1}{\partial x} + \lambda (u_2 - u_1), \\[2mm]
\dfrac{\partial (\alpha_1 \rho_1 E_1)}{\partial t} + \dfrac{\partial (\alpha_1 (\rho_1 E_1 + p_1) u_1)}{\partial x} = p_I u_I \dfrac{\partial \alpha_1}{\partial x} - \mu p_I'(p_1 - p_2) + \lambda u_I' (u_2 - u_1), \\[2mm]
\dfrac{\partial (\alpha_2 \rho_2)}{\partial t} + \dfrac{\partial (\alpha_2 \rho_2 u_2)}{\partial x} = 0, \\[2mm]
\dfrac{\partial (\alpha_2 \rho_2 u_2)}{\partial t} + \dfrac{\partial (\alpha_2 (\rho_2 u_2^2 + p_2))}{\partial x} = p_I \dfrac{\partial \alpha_2}{\partial x} - \lambda (u_2 - u_1), \\[2mm]
\dfrac{\partial (\alpha_2 \rho_2 E_2)}{\partial t} + \dfrac{\partial (\alpha_2 (\rho_2 E_2 + p_2) u_2)}{\partial x} = p_I u_I \dfrac{\partial \alpha_2}{\partial x} + \mu p_I'(p_1 - p_2) - \lambda u_I' (u_2 - u_1).
\end{cases}
\tag{2.1}
$$

The notations are conventional in the two-phase flow literature. α_k, ρ_k, p_k, $E_k = e_k + \frac{1}{2} u_k^2$ denote
respectively the volume fraction, density, pressure and total energy of phase k. e_k is the internal
energy and u_k represents the center of mass velocity of phase k. The mixture internal energy
is defined as $e = \sum_{k=1}^{2} Y_k e_k$ where $Y_k = (\alpha_k \rho_k)/\rho$ denotes the mass fraction of phase k. The
mixture density is defined as $\rho = \sum_{k=1}^{2} \alpha_k \rho_k$.

System (2.1) is a two-phase model for mixture flows evolving in pressure, velocity and
temperature disequilibria. The choice of interfacial average velocities u_I and pressures p_I
was originally expressed with the relations $u_I = u_2$ and $p_I = p_1$, the symmetric choice
$u_I = u_1$ and $p_I = p_2$, being possible as well.

More general and symmetric estimates have been proposed by Saurel et al. (2003) [15],

$$
\begin{cases}
u_I = u_I' + sgn\left(\dfrac{\partial \alpha_1}{\partial x}\right) \dfrac{p_2 - p_1}{Z_1 + Z_2}, & \text{with} \quad u_I' = \dfrac{Z_1 u_1 + Z_2 u_2}{Z_1 + Z_2}, \\[4mm]
p_I = p_I' + sgn\left(\dfrac{\partial \alpha_1}{\partial x}\right) \dfrac{(u_2 - u_1) Z_1 Z_2}{Z_1 + Z_2} & \text{with} \quad p_I' = \dfrac{Z_1 p_2 + Z_2 p_1}{Z_1 + Z_2},
\end{cases}
\tag{2.2}
$$

where $Z_k = \rho_k c_k$ is the acoustic impedance and c_k is the speed of sound of fluid k. This latter
is provided by a convex equation of state for each phase. The analysis which has led to these

estimates is based upon a homogenization method developed by Abgrall and Saurel (2003) [18]. Formulas (2.2) have been extended to 3D in Franquet and Perrier (2012) [19].

The first equation of System (2.1) is non-conservative and represents the transport of the first phase volume fraction α_1 at interfacial velocity u_I. During the advection stage, volume variations caused by pressure differences between the phases appear through the relaxation term $\mu(p_1 - p_2)$, with μ controlling the rate at which pressure equilibrium is reached. The above-mentioned analysis provided this coefficient as well $\mu = \frac{A_I}{Z_1 + Z_2}$ where A_I represents the specific interfacial area of the mixture. For instance, when dealing with clouds of droplets of radius R_1, the specific interfacial area is $A_I = \frac{3\alpha_1}{R_1}$.

The volume variations of the phases are then directly proportional to the pressure difference between the phases and the speed at which the equilibrium is reached is controlled by the μ coefficient. This latter depends only upon the acoustic impedance of the phases and upon the interfacial area.

The second and fifth equations of System (2.1) express the conservation of mass of the corresponding phase while the third and sixth equations are related to their momentum balance. Those relations are non-conservative. The velocity relaxation terms on the right-hand side of the momentum equations read $\pm \lambda \left(u_2 - u_1 \right)$, where λ is the product of the specific interfacial area with the drag coefficient. λ is a positive finite function (or tensor if there are more than two fluids). It controls the rate at which velocities tend towards equilibrium.

The non-conservative term $p_I \frac{\partial \alpha_1}{\partial x}$ represents the pressure force acting at the particle cloud boundaries with p_I denoting the interfacial pressure given by Eq. (2.2). This non-conservative term represents a "differential drag force" as its amplitude is high in zones of high volume gradients and vanishes when the volume fraction is uniform. It will be shown that this term is of main importance in the jet formation process.

Finally, the fourth and seventh equations of System (2.1) express the energy balance of phase k. Those latter ones are non-conservative as well due to the presence of the term $p_I u_I \frac{\partial \alpha_k}{\partial x}$ and the relaxation terms on the right-hand side.

System (2.1) is hyperbolic with wave speeds u_I, u_k and $u_k \pm c_k$ in the sense that all wave speeds (eigenvalues) are real but not necessarily distinct. Indeed, resonant situations may appear

such as for instance $u_2 = u_1 - c_1$, rendering impossible local determination of a full basis of eigenvectors. The reader is referred to Godlewski and Raviart (2013) [20] for details regarding the various levels of hyperbolicity. There is one additional wave in comparison with the original Baer and Nunziato's model (1986) [16] because of the interfacial velocity given by Eq. (2.2).

System (2.1) is closed by a convex equation of state (EOS) for each phase. Moreover, each phase admits the following entropy equation,

$$
\frac{\partial (\alpha_k \rho_k s_k)}{\partial t} + \frac{(\alpha_k \rho_k s_k u_k)}{\partial x} = \frac{1}{T_k (Z_k + Z_l)}
$$
$$
\times \left[Z_k (Z_k + Z_l)^{-1} \left[(p_l - p_k) + sgn\left(\frac{\partial \alpha_k}{\partial x}\right) (u_l - u_k) Z_l \right]^2 \left|\frac{\partial \alpha_k}{\partial x}\right| \right.
$$
$$
\left. + \mu Z_l (p_l - p_k)^2 + \lambda Z_k (u_l - u_k)(u_l - u_k), \right] \geq 0,
$$

(2.3)

where s_k and T_k denote respectively the specific entropy and temperature for each phase k. Index l denotes the conjugate phase to k, $i.e.$ $k = 1$ implies $l = 2$ and vice versa. Analyzing the right-hand side of Eq. (2.3), the second law of thermodynamics appears satisfied for each phase k. Thereby, the mixture entropy defined as $s = \sum_{k=1}^{2} (\alpha_k \rho_k s_k)$ fulfills the second law as well.

Consequently the model is hyperbolic, thermodynamically consistent and symmetric, in the sense that numbering of the fluids can be reversed, without changing the results. This feature is important when dealing with more than two phases. It is able to deal with contact and permeable interfaces, Saurel et al. (2003, 2014) [15], [21]. Its extension to more than two phases is possible [22]. However, the wave speeds are independent of the volume fraction, meaning that in the dilute limit the sound speed in the condensed phase is unchanged, this behavior being questionable as this phase is no longer continuous [23], [24], [25].

Indeed, with the BN-type model, the condensed phase sound speed corresponds to the one of the pure phase, while this phase is not continuous in the dilute limit and unable to propagate sound in reality, at least at a scale larger than a particle. When the phase is not continuous (dispersed drops in a gas, dispersed bubbles in a liquid), the associated sound speed should vanish, such effect being absent in the BN-type formulation.

8

This remark is the main motivation of the dense-dilute model of Saurel et al. (2017) [14] where the condensed phase does not propagate sound perturbations as soon as it is enough dispersed, typically $\alpha_1 < 0.5$, as there is no material support of the condensed phase to support sound.

In this direction an alternative formulation of the volume fraction equation is derived in the same reference, with the aim of improving the acoustic properties of Baer and Nunziato's model (1986) [16]. The model of Saurel et al. (2017) [14] is particularly attractive when one of the phases is dispersed and unable to support sound propagation (*i.e.* in dispersed liquid suspensions). Indeed, for liquid drops suspended in a gas or gas bubbles suspended in a liquid, the volume fraction of the dispersed phase α_1 in System (2.1) (first equation) is replaced by,

$$\frac{\partial \alpha_1}{\partial t} + \frac{\partial (\alpha_1 u_1)}{\partial x} = \mu(p_1 - p_2) \quad \text{with} \quad \mu \to +\infty. \tag{2.4}$$

The model of Saurel et al. (2017) [14] is presented in Section 4. First let us recall the model of Marble (1963) [17].

3. Dilute flow model

When the concentration of particles reaches the lower limit, the model of Marble (1963) [17] is preferred over the BN model,

$$\begin{cases} \dfrac{\partial \bar{\rho}_1}{\partial t} + \dfrac{\partial (\bar{\rho}_1 u_1)}{\partial x} = 0, \\[2mm] \dfrac{\partial (\bar{\rho}_1 u_1)}{\partial t} + \dfrac{\partial (\bar{\rho}_1 u_1^2)}{\partial x} = \lambda (u_2 - u_1), \\[2mm] \dfrac{\partial (\bar{\rho}_1 E_1)}{\partial t} + \dfrac{\partial (\bar{\rho}_1 E_1 u_1)}{\partial x} = \lambda u_I' (u_2 - u_1), \\[2mm] \dfrac{\partial \rho_2}{\partial t} + \dfrac{\partial (\rho_2 u_2)}{\partial x} = 0, \\[2mm] \dfrac{\partial (\rho_2 u_2)}{\partial t} + \dfrac{\partial (\rho_2 u_2^2 + p_2)}{\partial x} = -\lambda (u_2 - u_1), \\[2mm] \dfrac{\partial (\rho_2 E_2)}{\partial t} + \dfrac{\partial ((\rho_2 E_2 + p_2) u_2)}{\partial x} = -\lambda u_I' (u_2 - u_1). \end{cases} \tag{3.1}$$

System (3.1) corresponds to the Euler equations with source terms for the carrier phase (indexed 2) and pressureless gas dynamic equations for the dispersed phase (indexed 1), see also Zeldovich

9

(1970) [26]. The two phases are only linked through the $\lambda \left(u_2 - u_1 \right)$ term that represents viscous drag effects. Note that in System (3.1), $u'_I = u_1$ that corresponds to the velocity of the condensed phase, see Saurel et al. (1994, 2017) [27], [14].

The notations remain the same as before. In addition, the apparent density of the dispersed phase is introduced as $\bar{\rho}_1 = \alpha_1 \rho_1$. ρ_1 is the bulk density of the particles that are considered incompressible. ρ_1 remains consequently constant in System (3.1).

This flow model is valid only for dilute suspensions ($\alpha_1 < 0.01$) as volume fraction effects are omitted in the equations of the carrier phase and non-conservative terms are neglected (Rudinger (1965) [28]).

System (3.1) admits the following mixture entropy equation,

$$\frac{\partial \left(\bar{\rho}_1 s_1 + \rho_2 s_2 \right)}{\partial t} + \frac{\partial \left(\bar{\rho}_1 s_1 u_1 + \rho_2 s_2 u_2 \right)}{\partial x} = \lambda \frac{\left(u_1 - u_2 \right)^2}{T_2} \geq 0. \tag{3.2}$$

This model is consequently thermodynamically consistent. Moreover, the associated wave speeds are u_1, u_2, $u_2 - c_2$ and $u_2 + c_2$ where the eigenvalue u_1 is fourfold. The equations of the dilute phase are then hyperbolic linearly degenerate (or weakly hyperbolic), in the sense that all wave speeds are real but one is fold several times, rendering systematically impossible determination of a full basis of eigenvectors. Nevertheless the equations of the carrier phase are hyperbolic.

In this model, contrarily to the BN-type model (2.1), sound propagation is absent in the particle phase, this behavior being more physical in the dilute limit. However, Marble's model (3.1) has a limited range of validity as the volume of the dispersed phase is neglected, this assumption having sense only for low volume fractions (less than 1%) of the condensed phase.

4. Dense-dilute flow model

Recently, the gap between the BN-type (2.1) and Marble's (3.1) models has been filled (Saurel et al. (2017) [14]). Modifications of the volume fraction equation of Baer and Nunziato's model (1986) [16] in conjunction with stiff pressure relaxation resulted in a flow model where sound propagates only in the carrier phase, this behavior being more physical in the dilute limit. The

10

corresponding dense-dilute two-phase model reads,

$$
\begin{cases}
\dfrac{\partial \alpha_1}{\partial t} + \dfrac{\partial (\alpha_1 u_1)}{\partial x} = \mu (p_1 - p_2) \quad \text{with} \quad \mu \to +\infty, \\[2mm]
\dfrac{\partial (\alpha_1 \rho_1)}{\partial t} + \dfrac{\partial (\alpha_1 \rho_1 u_1)}{\partial x} = 0, \\[2mm]
\dfrac{\partial (\alpha_1 \rho_1 u_1)}{\partial t} + \dfrac{\partial (\alpha_1 (\rho_1 u_1^2 + p_1))}{\partial x} = p_1 \dfrac{\partial \alpha_1}{\partial x} + \lambda (u_2 - u_1), \\[2mm]
\dfrac{\partial (\alpha_1 \rho_1 E_1)}{\partial t} + \dfrac{\partial (\alpha_1 (\rho_1 E_1 + p_1) u_1)}{\partial x} = p_1 \dfrac{\partial (\alpha_1 u_1)}{\partial x} - \mu p_1 (p_1 - p_2) + \lambda u_I' (u_2 - u_1), \\[2mm]
\dfrac{\partial (\alpha_2 \rho_2)}{\partial t} + \dfrac{\partial (\alpha_2 \rho_2 u_2)}{\partial x} = 0, \\[2mm]
\dfrac{\partial (\alpha_2 \rho_2 u_2)}{\partial t} + \dfrac{\partial (\alpha_2 (\rho_2 u_2^2 + p_2))}{\partial x} = p_1 \dfrac{\partial \alpha_2}{\partial x} - \lambda (u_2 - u_1), \\[2mm]
\dfrac{\partial (\alpha_2 \rho_2 E_2)}{\partial t} + \dfrac{\partial (\alpha_2 (\rho_2 E_2 + p_2) u_2)}{\partial x} = -p_1 \dfrac{\partial (\alpha_1 u_1)}{\partial x} + \mu p_1 (p_1 - p_2) - \lambda u_I' (u_2 - u_1).
\end{cases}
\tag{4.1}
$$

Multiple estimates of the interfacial pressure and velocity are possible and thermodynamically consistent (see Saurel et al. (2017) [14]). For example, $p_I = (Z_2 p_1 + Z_1 p_2) / (Z_1 + Z_2)$ and $u_I' = (Z_1 u_1 + Z_2 u_2) / (Z_1 + Z_2)$ are admissible estimates. Those are identical to those of the BN-type model (Eq. (2.2)). Another admissible interface pressure estimate is $p_I = p_1$. This one is of interest as it yields determination of shock relations (Saurel et al. (2017) [14]). It is consequently used in the present paper. Regarding the interfacial velocity, both $u_I' = u_1$ and $u_I' = u_2$ are possible estimates and yield thermodynamic consistency. Following Carmouze et al. (2019) [13], $u_I' = u_1$ is used in the following.

The notations and mixture quantities are the same as before. Let us recall that phase 1 is considered as the dilute phase. System (4.1) evolves in velocity and temperature disequilibria and slight pressure disequilibrium in the sense that stiff pressure relaxation is required with this flow model. The asymptotic analysis provided in Saurel et al. (2017) [14] shows that System (4.1) recovers the mechanical-equilibrium two-phase flow model of Kapila et al. (2001) [29] when both stiff pressure and velocity relaxation processes are considered ($\mu, \lambda \to +\infty$).

In the present context $\mu \to +\infty$, meaning that instantaneous pressure relaxation is considered. Precise knowledge of μ is consequently of minor importance. As shown in Saurel et al. (2017) [14], this stiff pressure relaxation is necessary to ensure thermodynamic consistency. However, velocity relaxation may be considered at finite or instantaneous rates.

11

System (4.1) is hyperbolic with wave speeds u_1, u_2, $u_2 - c_2$ and $u_2 + c_2$ where the eigenvalue u_1 is fourfold. Its is consequently a hyperbolic degenerate system and the wave speeds of Marble's model (1963) [17] are recovered.

Compared to Marble's model (3.1), the dense-dilute one has two fundamental differences. The volume of the dispersed phase is considered and non-conservative terms are present in the momentum and energy equations. These non-conservative terms are often called "nozzling terms" (Bdzil et al. (1999) [30]) in reference to the Euler equations with variable cross section. We prefer however to interpret them as "differential drag force" as mentioned earlier.

The dense-dilute model of Saurel et al. (2017) [14] fills the gap between Marble's and Baer and Nunziato's models. It is a weakly hyperbolic system (a wave speed is fold several times) where sound propagates only in the carrier phase while being valid in the whole range of dispersed volume fraction. Is is also thermodynamically consistent as the entropy production is non-negative in the same stiff pressure relaxation limit.

Indeed, as shown in Saurel et al. (2017) [14], the entropy equation for the mixture, in the stiff pressure relaxation limit, reads:

$$\frac{\partial \left(\alpha_1 \rho_1 s_1 + \alpha_2 \rho_2 s_2 \right)}{\partial t} + \frac{\partial \left(\alpha_1 \rho_1 s_1 u_1 + \alpha_2 \rho_2 s_2 u_2 \right)}{\partial x} = \lambda \frac{\left(u_1 - u_2 \right)^2}{T_2} + \Theta \left(\epsilon \right) \geq 0 \quad \text{with} \quad \mu = \frac{1}{\epsilon} \to +\infty. \tag{4.2}$$

The $\Theta \left(\epsilon \right)$ term in the entropy source is related to pressure relaxation terms and vanishes in the limit $\epsilon = \frac{1}{\mu} \to 0^+$.

Compared to the BN-type model, the present one has three major differences:

– As already mentioned, sound propagation in the dispersed phase is absent;

– Density variations of the dispersed phase come from pressure relaxation only and not from velocity divergence. In other words, when two particles move away or get closer, their densities remain constant along their trajectories, while they vary in the BN-type model. As the particles are dispersed, there is no reason for their densities to vary. With the present model, this behavior is reproduced as a consequence of the combination of the

12

volume fraction and mass balance equations of the dispersed phase (Saurel et al. (2017) [14]).

210 – At the end of the pressure relaxation process, mandatory with the present model, the solution is projected onto a hyperbolic surface. With the BN-type model, it is projected onto a conditionally hyperbolic surface, where eigenvalues are possibly complex numbers, as for all models based on conventional balance equations and pressure equilibrium condition among the phases (see for example Ghidaglia et al. (2001) [31]).

215 Recently the authors developed in Carmouze et al. (2019) [13] a simple and accurate Riemann solver with internal reconstruction (RSIR) for this specific model. Thanks to the RSIR solver and as a consequence of better acoustic properties of the dilute phase, this model is able to reproduce, at least qualitatively, finger-like instabilities reminiscent of particle jetting during radial explosion.

220 We believe that the formation mechanism of this fingering instability is closely related to the non-conservative terms of the present dense-dilute model (System (4.1)). They play the role of a "differential drag force", acting intensively at cloud boundaries and vanishing in the wake, when volume fraction gradients disappear.

Despite the contribution of viscous drag effects for flow involving clouds of drops, bubbles, or 225 granular beds, we believe that viscous drag effects are not at the origin of finger-like instabilities.

This observation is investigated deeper in the present paper. Comparisons of System (2.1) (variant of Baer and Nunziato's (1986) [16] model), System (3.1) (Marble's (1963) [17] model) and System (4.1) (dense-dilute model of Saurel et al. (2017) [14]) are provided. Only the dense-dilute model seems to be able to reproduce such finger-like instabilities with or without viscous 230 drag effects. Their modeling is addressed hereafter.

5. Viscous drag effects

The viscous drag parameter λ present in Systems (2.1), (3.1) and (4.1) controls the rate at which velocity equilibrium is reached. The $\lambda(\mathbf{u}_2 - \mathbf{u}_1)$ term represents the viscous drag force and $\lambda\mathbf{u}'_I.(\mathbf{u}_2 - \mathbf{u}_1)$ the power of this force (per unit volume).

Let us denote this force as $n_p \, \mathbf{F}_{g \to p}$ where n_p represents the specific number of particles. For the sake of simplicity the particles are considered spherical in this work and viscous drag effects are treated via the following relation due to Stokes,

$$\mathbf{F}_{g \to p} = 6\pi \, \mu_2 \, R_1 \left(\mathbf{u}_2 - \mathbf{u}_1 \right), \tag{5.1}$$

where R_1 is the radius of the particles considered constant in this work and μ_2 the kinematic viscosity of the carrier phase.

Let us now denote the particle Reynolds number as,

$$Re_p = \frac{2R_1 \rho_2 |\mathbf{u}_1 - \mathbf{u}_2|}{\mu_2}. \tag{5.2}$$

It is important to note that such viscous drag representation is only valid for low Reynolds numbers. In such conditions the viscous drag coefficient reads $C_d = \frac{24}{Re_p}$.

With the help of the previous relations, the viscous drag force can be written concisely as,

$$\mathbf{F}_{g \to p} = \frac{C_d R_1^2 \, \pi \, \rho_2}{2} |\mathbf{u}_1 - \mathbf{u}_2| \left(\mathbf{u}_2 - \mathbf{u}_1 \right). \tag{5.3}$$

In order to extend the present viscous drag law to higher Reynolds numbers, the viscous drag coefficient is reconsidered to account for turbulent effects following Naumann and Schiller (1935) [32],

$$C_d = \begin{cases} \dfrac{24}{Re_p} \left(1 + 0.15 Re_p^{0.687} \right) & \text{if} \quad Re_p < 800, \\[2ex] 0.438 & \text{otherwise.} \end{cases} \tag{5.4}$$

As the particles are considered spherical with a constant radius R_1, the number of particles reads $n_p = \frac{\alpha_1}{\frac{4}{3}\pi R_1^3}$, and the total viscous drag force in a control volume becomes,

$$n_p \, \mathbf{F}_{g \to p} = \frac{3}{8R_1} \alpha_1 C_d \rho_2 |\mathbf{u}_1 - \mathbf{u}_2| \left(\mathbf{u}_2 - \mathbf{u}_1 \right), \tag{5.5}$$

that is to say,

$$n_p \, \mathbf{F}_{g \to p} = \lambda \left(\mathbf{u}_2 - \mathbf{u}_1 \right) \quad \text{with} \quad \lambda = \frac{3}{8R_1} \alpha_1 C_d \rho_2 |\mathbf{u}_1 - \mathbf{u}_2|. \tag{5.6}$$

14

To express the power of the viscous drag force, expression of the interfacial velocity is required. Following Saurel et al. (2003) [15] the interfacial velocity is determined as $\mathbf{u}'_I = \frac{Z_1\mathbf{u}_1+Z_2\mathbf{u}_2}{Z_1+Z_2}$ for System (2.1) evolving in total disequilibrium. Systems (3.1) and (4.1), corresponding to Marble's and dense-dilute models, use directly $\mathbf{u}'_I = \mathbf{u}_1$ as interfacial velocity. This assumption is indeed admissible and yields thermodynamic consistency (see Saurel et al. (2017) [14]). In the present context, as $Z_1 \gg Z_2$, there is no significant difference between the two models for $\mathbf{u}'_I$.

6. Particle jetting during radial explosion

In the present paper, computations are based on the flow models (2.1), (3.1) and (4.1) considered in 2D and resolved numerically in the DALPHADT$^{©}$ code on unstructured triangular cells. A Godunov-type method including non-conservative terms is used and extended to second order with the MUSCL-type method presented in Chiapolino et al. (2017) [33].

The BN-type model (2.1) is solved with the help of the HLLC-type solver of Furfaro and Saurel (2015) [34]. Marble's model (3.1) is solved with the Riemann solver of Saurel et al. (1994) [27]. The dense-dilute model (4.1) is solved via the RSIR solver developed in Carmouze et al. (2019) [13].

In the following a configuration like the one considered in Rodriguez et al. (2013) [7] with a Hele-Shaw cell and a particle ring is studied. This configuration has been studied in Carmouze et al. (2019) [13] as well. The numerical domain consists in a portion of a complete disc where a particle bed is initially at rest. Wall boundary conditions are considered for symmetry reasons except at the far-right boundary that is non-reflective. The initial conditions are schematically depicted in Fig. 3. The initial data are reported in Table 1. The Stiffened-Gas (SG) EOS, $p_k = (\gamma_k - 1)\rho_k e_k - \gamma_k p_{\infty,k}$, is used for the sake of simplicity [35]. The dilute phase is made of solid particles, treated as compressible material, governed by the SG EOS with the same parameters as liquid water: $\gamma_1 = 4.4$ and $p_{\infty,1} = 6 \cdot 10^8$ Pa, while air is used as carrier phase with $\gamma_2 = 1.4$. Liquid water parameters are used for the sake of simplicity. In the present pressure range, density of the condensed phase has weak variations and the EOS parameters are not important, provided $p_{\infty,1} \gg 1$. This is similar to the one-dimensional numerical simulations of Saurel et al. (2017) [14] where Rogue's (1998) [36] experiments are addressed, validating the

dense-dilute model (4.1). In this reference, the experiment consists in the fluidization in a shock tube of a nylon particle cloud under shock wave interaction.
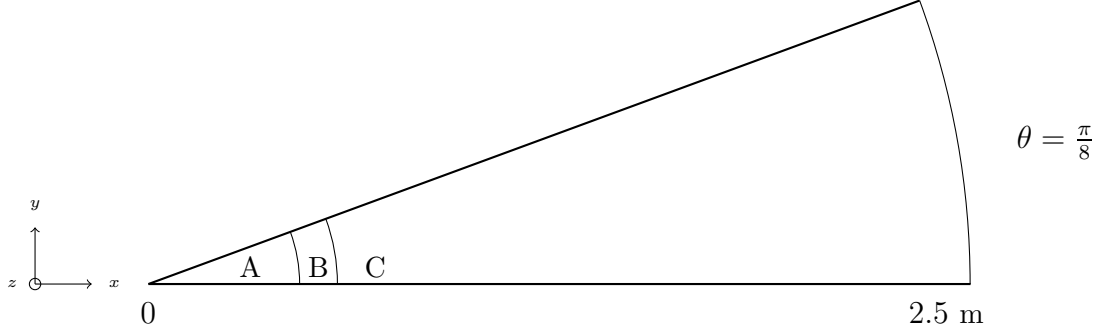

Figure 3: Schematic representation of the computational domain of the particle jetting test. The portion represents 1/16 of a complete disc with angle $\theta = \pi/8$. The domain denoted A corresponds to the high-pressure chamber, filled with gas. The domain denoted B represents the initial particle ring. It is located at $x = 0.5$ m and is 4-cm wide. The domain C corresponds to the low-pressure chamber at atmospheric conditions. The use of triangular cells enables clear definition of the particle ring. No mixed cell is present initially, meaning that no initial wavelength or perturbation is introduced (see Carmouze et al. (2019) [13]). Initial data are reported in Table 1. The boundaries are considered as walls (symmetry condition) except for the far-right one considered as non-reflective.

Domain	A	B	C
α_1	0.0001	0.4	0.0001
ρ_1 (kg.m^{-3})	1050	1050	1050
ρ_2 (kg.m^{-3})	12	1.2	1.2
$u_1 = u_2$ (m.s^{-1})	0	0	0
$p_1 = p_2$ (Pa)	10^7	10^5	10^5

Table 1: Initial data of the particle jetting test schematically depicted in Fig. 3.

Stiff pressure relaxation is used (Lallemand and Saurel (2000) [37]) for System (2.1) and System (4.1). The diameter of the particles is constant and set to $D_1 = 1$ mm. The gas viscosity is $\mu_2 = 18 \cdot 10^{-6}$ Pa·s. The initial data do not involve any perturbation or wavelength. The volume fractions and densities are constant in the granular bed.

6.1. BN-type model with viscous drag effects

First, the BN-type (2.1) model is used. The corresponding results are shown at different times in Fig. 4 as volume fraction contours.
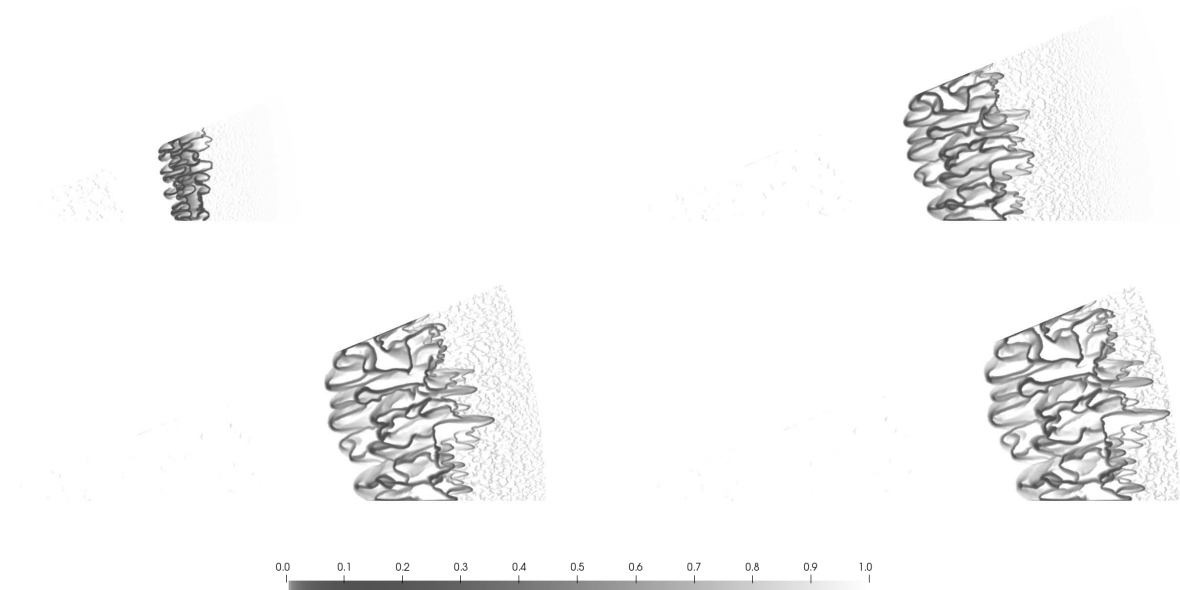
16

Figure 4: Volume fraction contours of the dispersed phase for the particle jetting simulation with the BN-type model (2.1). Viscous drag effects are present. Stiff pressure relaxation is considered. Results are obtained with the HLLC solver of Furfaro and Saurel (2015) [34] embedded in the MUSCL-type scheme [33] with Sweby's limiter and $\Phi = 1.5$ (Eq. 3.17 of [38]). Results are shown at times $t = 1.5$ ms, $t = 3$ ms, $t = 3.75$ ms and $t = 4.1$ ms. The mesh is made of $723,152$ triangular elements. The CFL number is 0.5.

Cellular structures appear in Fig. 4 but they do not correspond qualitatively to the experimental observations reported in Fig. 2. In particular, inner and outer fingers seem absent.

6.2. Dilute model with viscous drag effects

Marble's model (3.1) is now considered. Results with the same mesh and at the same times as previously are provided in Fig. 5. The same viscous drag force with the same parameters is used in both computations. Note that the same initial conditions as before are used (Table 1). As initially $\alpha_1 = 0.4$ within the particle ring, Marble's model (3.1) is used outside its range of validity ($\alpha_1 < 0.01$).

However $\alpha_1 = 0.4$ is in agreement with the experimental initial conditions of Rodriguez et al. (2013) [7]. As only qualitative results are aimed in the present paper, this set of initial conditions is not problematic. The aim of the present computation is to show the effect of viscous drag force only, compared to the previous computation (Fig. 4) where both viscous drag and non-conservative terms are present.
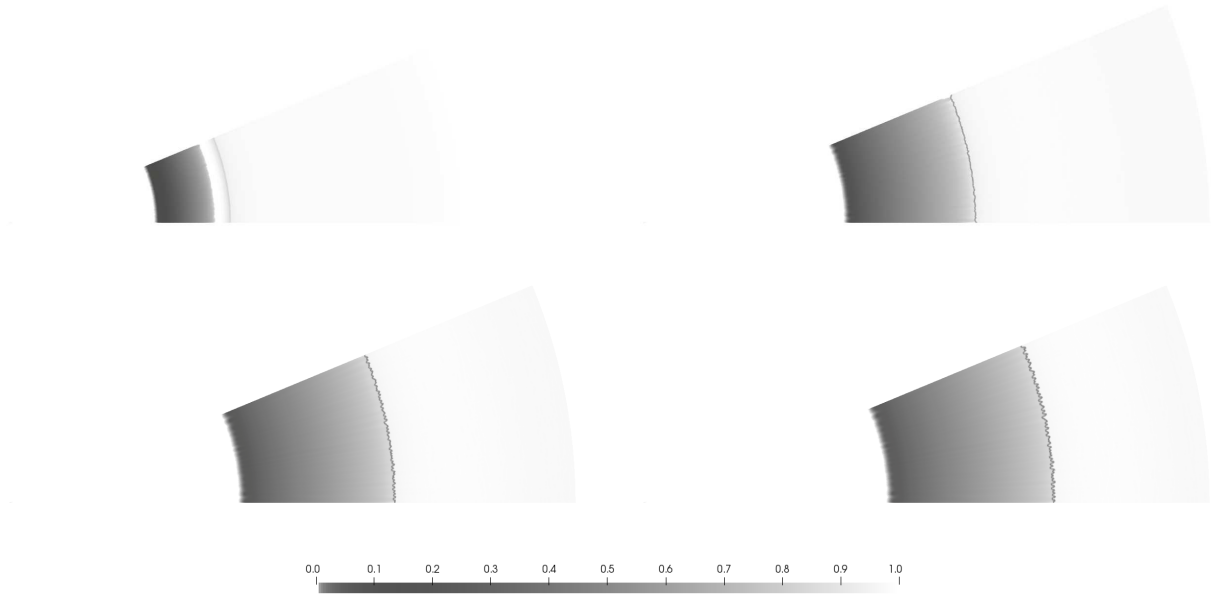
17

Figure 5: Volume fraction contours of the dispersed phase for the particle jetting simulation with Marble's model (3.1). Viscous drag effects are present. Results are obtained with the Riemann solver of Saurel et al. (1994) [27] embedded in the MUSCL-type scheme [33] with Sweby's limiter and $\Phi = 1.5$ (Eq. 3.17 of [38]). Results are shown at times $t = 1.5$ ms, $t = 3$ ms, $t = 3.75$ ms and $t = 4.1$ ms. The mesh is made of $723,152$ triangular elements. The CFL number is 0.5.

300   Computed results of Fig. 5 show that inner and outer jet instabilities are absent in the present computation. When the test is continued on larger scales in both time and space, no instability appears.

These results show that:

– Marble's model is inappropriate to address finger-type instabilities;

305   – Viscous drag force effects are not responsible for their appearance.

6.3. Dense-dilute model with viscous drag effects

The dense-dilute model (4.1) is now considered. Results with the same mesh and at the same times as previously are shown in Fig. 6.
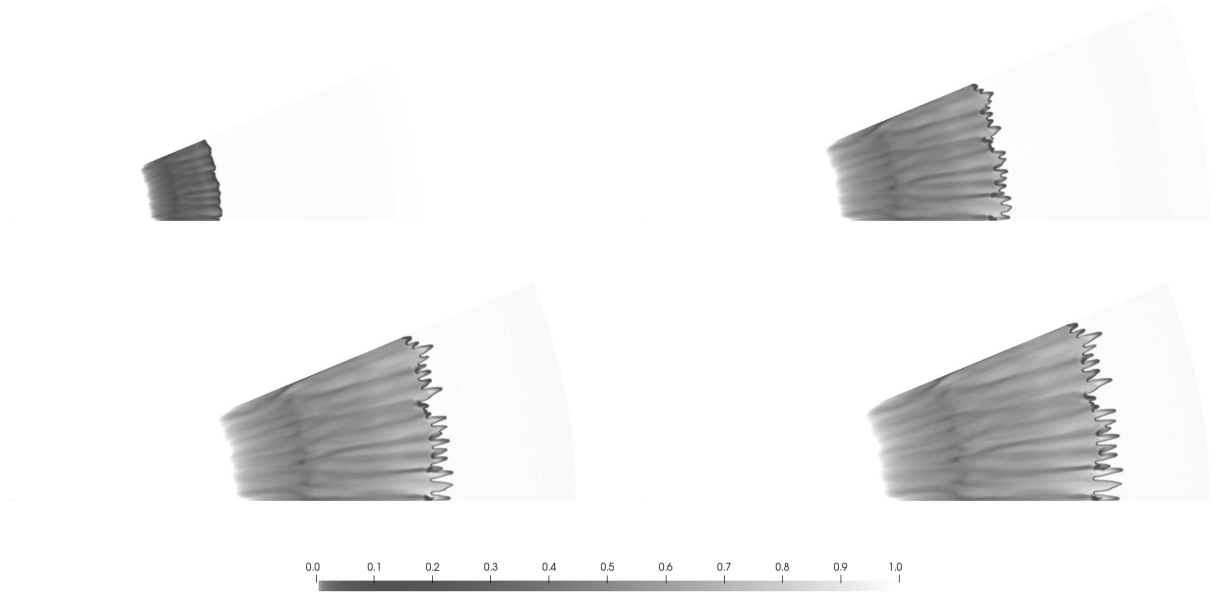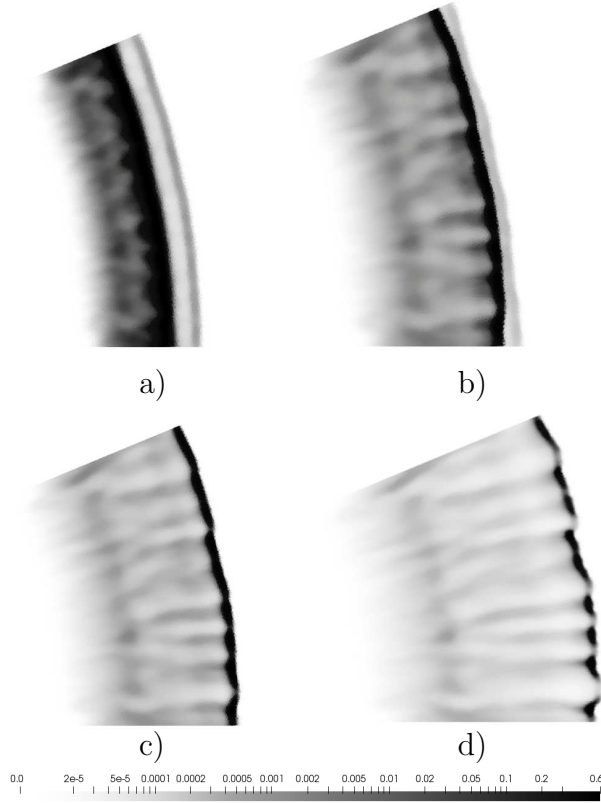
18

Figure 6: Volume fraction contours of the dispersed phase for the particle jetting simulation with the dense-dilute model (4.1). Viscous drag effects are present. Stiff pressure relaxation is considered. Results are obtained with the RSIR solver of Carmouze et al. (2019) [13] embedded in the MUSCL-type scheme [33] with Sweby's limiter and $\Phi = 1.5$ (Eq. 3.17 of [38]). Results are shown at times $t = 1.5$ ms, $t = 3$ ms, $t = 3.75$ ms and $t = 4.1$ ms. The mesh is made of $723,152$ triangular elements. The CFL number is 0.5.

Finger-like instabilities are produced at the inner and outer cloud boundaries, at least quali-
tatively. Let us now investigate the early stages of the instability formation. Related computed results are shown in Fig 7.

19

Figure 7: Volume fraction contours of the dispersed phase for the particle jetting simulation with the dense-dilute model (4.1) focused on the particle cloud at early times: a) $t = 0.6$ ms, b) $t = 0.84$ ms, c) $t = 1$ ms and d) $t = 1.3$ ms. In the present figure, the scale is adapted for each result for the sake of clarity. Viscous drag effects are present. Stiff pressure relaxation is considered. Results are obtained with the RSIR solver of Carmouze et al. (2019) [13] embedded in the MUSCL-type scheme [33] with Sweby's limiter and $\Phi = 1.5$ (Eq. 3.17 of [38]). The mesh is made of $723,152$ triangular elements. The CFL number is 0.5. A compaction zone appears first in the cloud in the darkest zone. Particle jets develop at the inner interface and direct to the domain center. Their growth is visible by comparing their length in graphs (a) and (b). They qualitatively look like the instabilities observed in Fig. 2 (a) and (b). Another front emerges at the outer surface but appears more like a diffusion zone rather than the short wavelength instabilities visible in Fig. 2 (b). Eventually the two fronts merge in graph (c) and the resulting front at the outer boundary starts to destabilize in graph (d).

In Fig. 7 internal jets appear and develop to the center domain direction. A compaction zone appears in the cloud and a detached front with low particle concentration also appears ahead of the compaction front. Noticeably, the compaction front in the darkest zone catches up the detached front and starts to destabilize. Evolution at intermediate times is reported in Fig. 8.
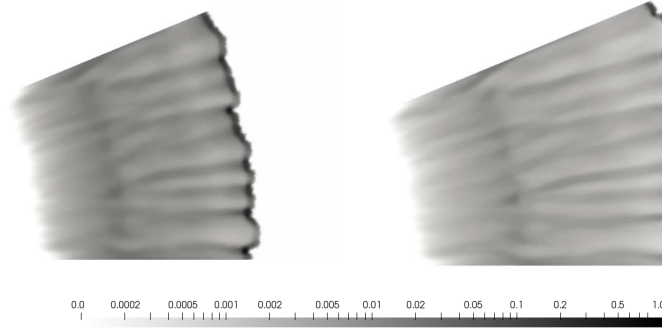
Figure 8: Volume fraction contours of the dispersed phase for the particle jetting simulation with the dense-dilute model (4.1) focused on the particle cloud at intermediate times: $t = 1.5$ ms and $t = 2.25$ ms. In the present figure, the scale is adapted for each result for the sake of clarity. Viscous drag effects are present. Stiff pressure relaxation is considered. Results are obtained with the RSIR solver of Carmouze et al. (2019) [13] embedded in the MUSCL-type scheme [33] with Sweby's limiter and $\Phi = 1.5$ (Eq. 3.17 of [38]). The mesh is made of $723, 152$ triangular elements. The CFL number is 0.5. The compaction front and the detached one are now merged and destabilize. Particle concentration zones having cluster-type shapes appear in the graph on the right ($t = 2.25$ ms). Inner jets are still present and keep on developing.

In Fig. 8 the external front destabilizes, and relatively dense particle clusters appear. The inner front jets flowing to the domain center continue their development. Evolution at later times is reported in Fig. 9.
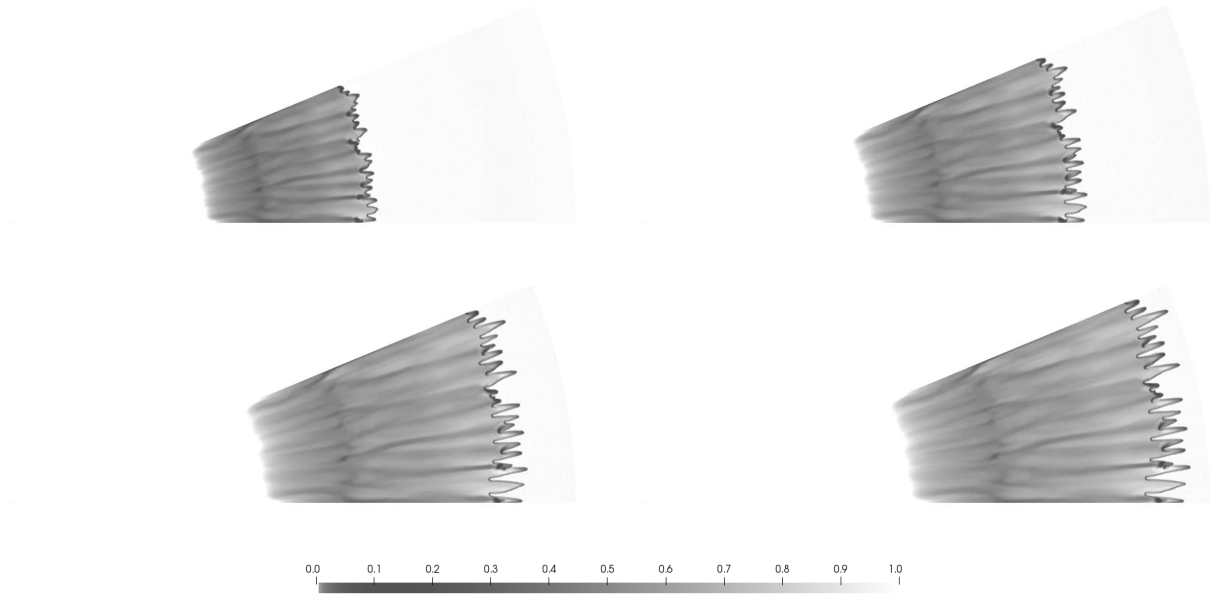
Figure 9: Volume fraction contours of the dispersed phase for the particle jetting simulation with the dense-dilute model (4.1). Viscous drag effects are present. Stiff pressure relaxation is considered. Results are obtained with the RSIR solver of Carmouze et al. (2019) [13] embedded in the MUSCL-type scheme [33] with Sweby's limiter and $\Phi = 1.5$ (Eq. 3.17 of [38]). Results are shown at times $t = 3.0$ ms, $t = 3.75$ ms, $t = 4.5$ ms and $t = 4.8$ ms. The mesh is made of $723,152$ triangular elements. The CFL number is 0.5. External front instabilities are now created and develop. Dilution of the internal jets happens while external jets develop as a consequence of particle "dense" zones created at intermediate times. External jets' amplitude grows as seen by comparing the different results.

In Fig. 9 external front instabilities are created and develop while internal ones tend to vanish. Although not precisely identified from the present numerical experiments, the formation mechanism of this fingering instability appears closely related to the non-conservative terms. They play the role of a "differential drag force", acting intensively at cloud boundaries and vanishing in the wake, when volume fraction gradients disappear.

At the modeling level, non-conservative terms present similarities with capillary ones (Brackbill et al. (1992) [39], Perigaud and Saurel (2005) [40]) except that curvature effects are absent in the present two-phase formulation. Another major difference is that cloud boundaries are obviously highly permeable in the present context, while interfaces are not permeable in conventional hydrodynamic instabilities, except those considering flames and phase transition, where low permeability is present compared to the present configuration.

The magnitude of the "differential drag force" appearing through the non-conservation terms

22

is compared in Fig. 10 to the conventional viscous drag force. The results correspond to those of Fig. 9 at time $t = 4.8$ ms. The purpose of Fig. 10 is not to provide precise values of the corresponding drag forces but to highlight the importance of the "differential drag force". The ratio $\frac{p_I|grad(\alpha_1)|}{\lambda|\mathbf{u}_2-\mathbf{u}_1|}$ is then plotted (when defined) in the surrounding area of the fingers along the radius of the computational domain along the angle $\frac{\pi}{16}$ (Fig. 3).
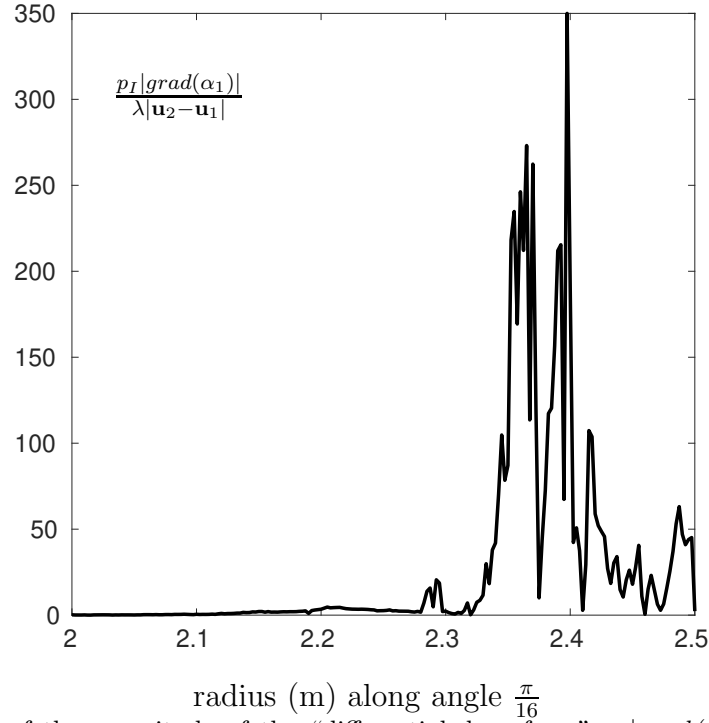

radius (m) along angle $\frac{\pi}{16}$

Figure 10: Comparison of the magnitude of the "differential drag force" $p_I|grad(\alpha_1)|$ and the conventional viscous drag force $\lambda|\mathbf{u}_2 - \mathbf{u}_1|$. The present results correspond to those of Fig. 9 at time $t = 4.8$ ms. The ratio $\frac{p_I|grad(\alpha_1)|}{\lambda|\mathbf{u}_2-\mathbf{u}_1|}$ is plotted (when defined) in the vicinity of the fingers (between 2 m and 2.5 m in the present figure). The abscissa corresponds to the radius of the computational domain along the angle $\frac{\pi}{16}$ (Fig. 3).

The previous results show the importance of the "differential drag force" and strengthens the idea that the fingering instability is closely related to the non-conservative terms. In the surroundings of the fingers, the "differential drag force" $p_I|grad(\alpha_1)|$ is about 100 times larger than the conventional viscous drag force $\lambda|\mathbf{u}_2 - \mathbf{u}_1|$. Contribution of the non-conservative terms alone will be addressed in Section 6.4 by removing viscous drag effects ($\lambda = 0$). It will be seen that finger-like instabilities appear nonetheless.

First, let us address spatial resolution effects. It appears that the number of created fingers

is mesh independent. Indeed, as shown in Fig. 11, the same number of fingers is created with four different meshes.
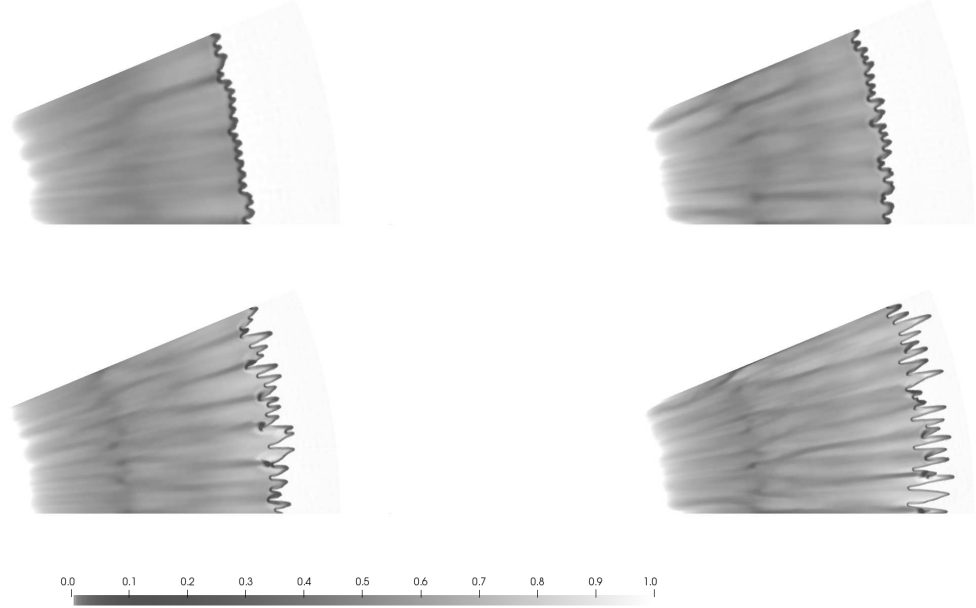

Figure 11: Volume fraction contours of the dispersed phase for the particle jetting simulation with the dense-dilute model (4.1). Study of mesh resolution effects. Viscous drag effects are present. Stiff pressure relaxation is considered. Results are obtained with the RSIR solver of Carmouze et al. (2019) [13] embedded in the MUSCL-type scheme [33] with Sweby's limiter and $\Phi = 1.5$ (Eq. 3.17 of [38]). Results are shown at $t = 4.8$ ms with four different meshes, $240,672$ cells, $361,222$ cells, $539,354$ cells and $723,152$ cells. The CFL number is 0.5.

Obviously, mesh resolution influences jets' shape and length, as numerical diffusion is present. However, it does not change the number of jets and their qualitative shape, meaning that this instability is "robust" and that the flow model and present numerical method seem appropriate for their study.

6.4. Dense-dilute model without viscous drag effects

In order to isolate the contribution of the non-conservative terms, the previous test is rerun with the dense-dilute model (4.1) and in the absence of viscous drag effects ($\lambda = 0$). Stiff pressure relaxation remains active nonetheless.

Computed results are shown at various times in Fig. 12. Those show that finger-like instabilities are produced without considering viscous drag effects.
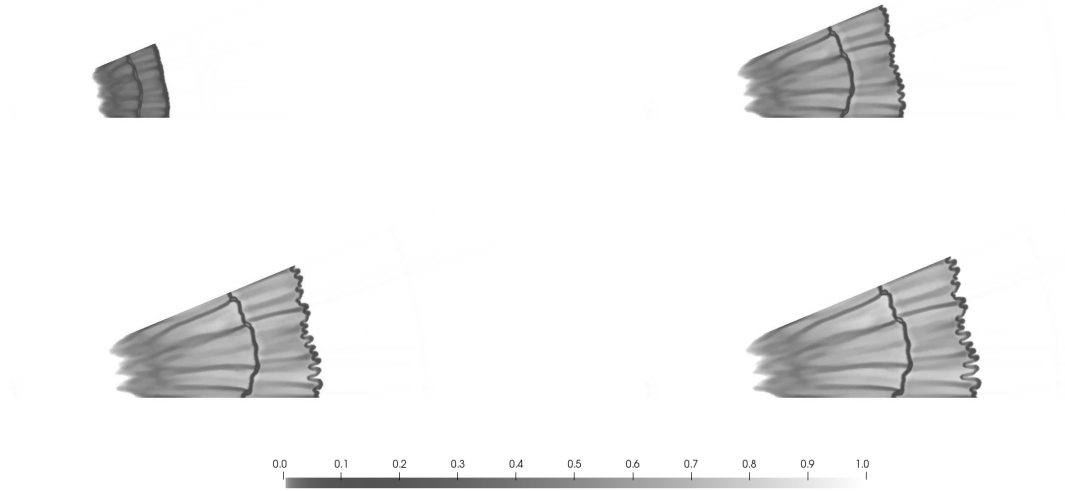
24

Figure 12: Volume fraction contours of the dispersed phase for the particle jetting simulation with the dense-dilute model (4.1). Viscous drag effects are absent. Stiff pressure relaxation is considered. Results are obtained with the RSIR solver of Carmouze et al. (2019) [13] embedded in the MUSCL-type scheme [33] with Sweby's limiter and $\Phi = 1.5$ (Eq. 3.17 of [38]). Results are shown at times $t = 1.5$ ms, $t = 3$ ms, $t = 3.75$ ms and $t = 4.1$ ms. The mesh is made of $723,152$ triangular elements. The CFL number is 0.5. The present results are to be compared to those of Fig. 6 where viscous drag effects are present.

³⁵⁵   Finger-like instabilities appear despite the absence of viscous drag effects. Viscous drag effects have contribution nonetheless as seen by comparing Fig. 6 (with viscous drag effects) and Fig. 12 (without viscous drag effects). However, according to the present results, the origin of finger-like instabilities does not depend on viscous drag.

This observation is mesh independent as shown in Fig. 13 where four different meshes are ³⁶⁰ used, always yielding the same conclusion.
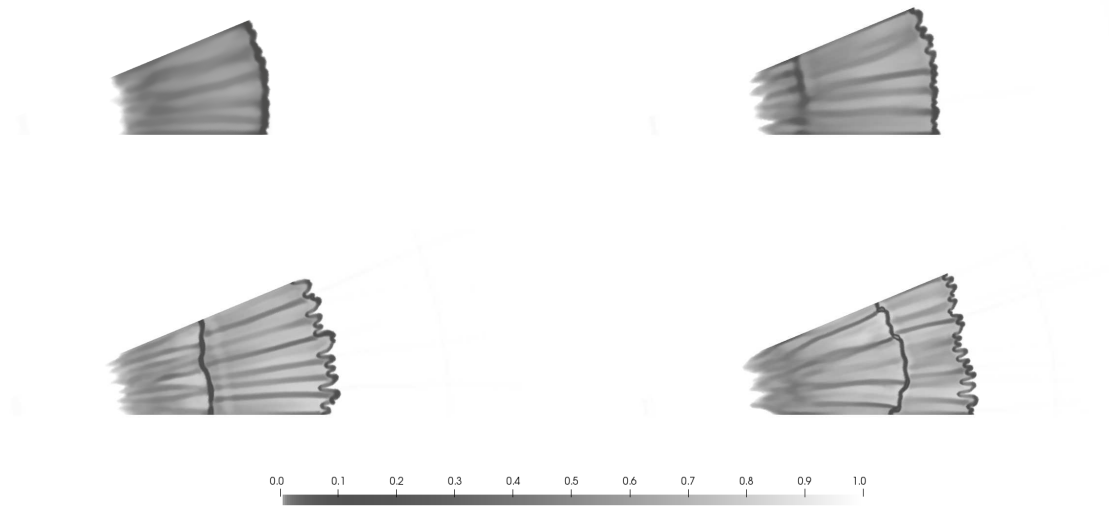
Figure 13: Volume fraction contours of the dispersed phase for the particle jetting simulation with the dense-dilute model (4.1). Study of mesh resolution effects. Viscous drag effects are absent. Stiff pressure relaxation is considered. Results are obtained with the RSIR solver of Carmouze et al. (2019) [13] embedded in the MUSCL-type scheme [33] with Sweby's limiter and $\Phi = 1.5$ (Eq. 3.17 of [38]). Results are shown at $t = 4.1$ ms with four different meshes, $240,672$ cells, $361,222$ cells, $539,354$ cells and $723,152$ cells. The CFL number is 0.5.

Same type of computations is now addressed on plane geometry, to remove radial flow divergence effects.

6.5. Dense-dilute model with viscous drag effects on plane geometry

The same particle cloud as before is considered on a plane configuration. The dimensions are similar to the ones of the previous test. The domain is 2.5-m long and 0.478-m wide. The particle bed is located at $x = 0.5$ m and is 4-cm wide.

Computed results are shown in Fig. 14. Instabilities appear at the inner and outer boundaries but their qualitative shape is significantly different. Finger-like jets are absent, as reported in the shock tube experiments of Chauvin (2012) [41], and are more replaced by mixing zones.
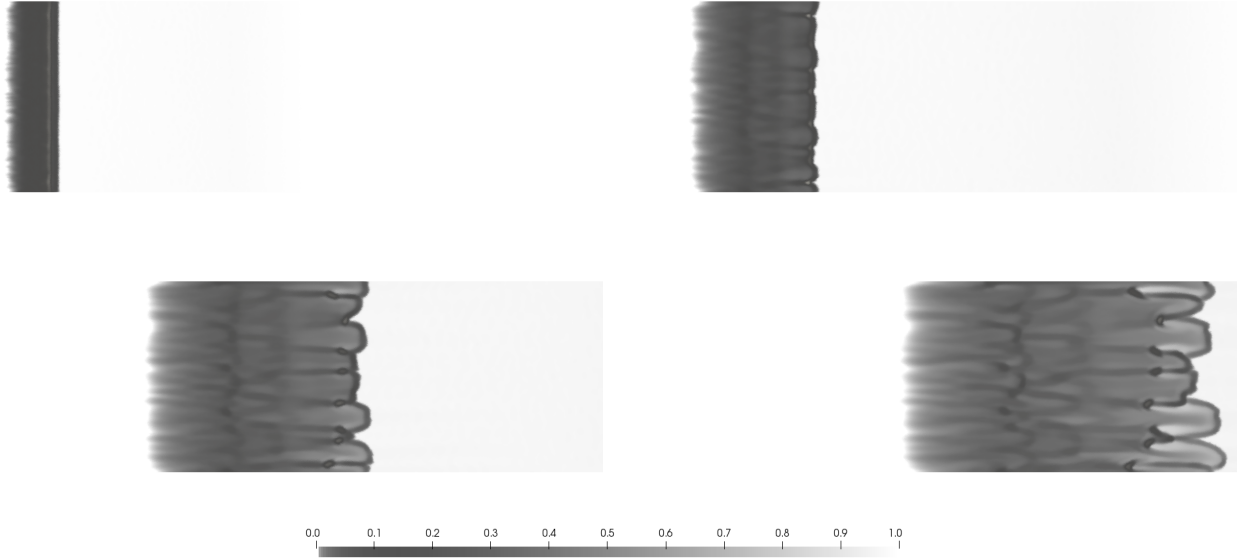
26

Figure 14: Volume fraction contours of the dispersed phase for the particle jetting simulation with the dense-dilute model (4.1) on a plane geometry. Viscous drag effects are present. Stiff pressure relaxation is considered. Results are obtained with the RSIR solver of Carmouze et al. (2019) [13] embedded in the MUSCL-type scheme [33] with Sweby's limiter and $\Phi = 1.5$ (Eq. 3.17 of [38]). Results are shown at times $t = 0.75$ ms, $t = 1.5$ ms, $t = 2.25$ ms and $t = 3$ ms. The mesh is made of 352.262 triangular elements. The CFL number is 0.5. The domain is 2.5-m long and 0.478-m wide. The particle bed is located at $x = 0.5$ m and is 4-cm wide.

It therefore appears that radial divergence effects are important in the appearance of this instability.

7. Conclusion

Various hyperbolic two-phase flow models have been tested for the computation of particle finger-like instabilities. Three main conclusions emerge from the present analysis:

– The only flow model able to predict qualitatively these instabilities is the dense-dilute two-phase model of Saurel et al. (2017) [14];

– Formation of this instability is not related to viscous drag effects but more to "differential drag" modeled through non-conservative terms in the momentum and energy equations;

– The instability requires radial flow divergence, present in cylindrical and spherical explosions, but absent in plane configurations.

27

The instability formation mechanism is still unidentified, but the flow model as well as precise effects (differential drag) are now identified for deeper investigations.

In memoriam

This paper is dedicated to the memory of Dr. Douglas Nelson Woods (*January 11$^{\text{th}}$ 1985 - †September 11$^{\text{th}}$ 2019), promising young scientist and post-doctoral research fellow at Los Alamos National Laboratory. Our thoughts and wishes go to his wife Jessica, to his parents Susan and Tom, to his sister Rebecca and to his brother Chris, whom he left behind.

References

[1] F. Zhang, D. Frost, P. Thibault, S. Murray, Explosive dispersal of solid particles, Shock Waves 10 (6) (2001) 431–443.

[2] A. Milne, C. Parrish, I. Worland, Dynamic fragmentation of blast mitigants, Shock Waves 20 (1) (2010) 41–51.

[3] D. Frost, S. Goroshin, F. Zhang, Jet formation during explosive particle dispersal, Proceedings of the 21st Military Aspects of Blast and Shock, Jerusalem, Israel (2010).

[4] C. Parrish, I. Worland, Dynamic jet formation from mitigation materials, in: 28th International Symposium on Shock Waves, Springer, 2012, pp. 107–113.

[5] A. Osnes, M. Vartdal, M. Omang, B. Reif, Numerical investigation of shock wave particle cloud interaction in cylindrical geometries, arXiv preprint arXiv:1906.06709 (2019).

[6] P. Utkin, Numerical simulation of shock wave–dense particles cloud interaction using Godunov solver for Baer–Nunziato equations, International Journal of Numerical Methods for Heat & Fluid Flow 29 (9) (2019) 3225–3241.

[7] V. Rodriguez, R. Saurel, G. Jourdan, L. Houas, Solid-particle jet formation under shock-wave acceleration, Physical Review E 88 (6) (2013) 063011.

[8] K. Xue, K. Du, X. Shi, Y. Gan, C. Bai, Dual hierarchical particle jetting of a particle ring undergoing radial explosion, Soft matter 14 (22) (2018) 4422–4431.

[9] T. McGrath, J. Clair, S. Balachandar, Modeling compressible multiphase flows with dispersed particles in both dense and dilute regimes, Shock Waves 28 (3) (2018) 533–544.

[10] A. Osnes, M. Vartdal, B. Reif, Numerical simulation of particle jet formation induced by shock wave acceleration in a Hele-Shaw cell, Shock Waves 28 (3) (2018) 451–461.

[11] Q. Carmouze, F. Fraysse, R. Saurel, B. Nkonga, Coupling rigid bodies motion with single phase and two-phase compressible flows and unstructured meshes, Journal of Computational Physics 375 (2018) 1314–1338.

[12] V. Rodriguez, Etude de la formation de jets issus de la dispersion d'un anneau de particules solides par onde de choc, Ph.D. thesis, Aix-Marseille University (2014).

[13] Q. Carmouze, R. Saurel, A. Chiapolino, E. Lapébie, Riemann solver with internal reconstruction (RSIR) for compressible single-phase and non-equilibrium two-phase flows, Journal of Computational Physics (2019) 109176.

[14] R. Saurel, A. Chinnayya, Q. Carmouze, Modelling compressible dense and dilute two-phase flows, Physics of Fluids 29 (6) (2017) 063301.

[15] R. Saurel, S. Gavrilyuk, F. Renaud, A multiphase model with internal degrees of freedom: Application to shock–bubble interaction, Journal of Fluid Mechanics 495 (2003) 283–321.

[16] M. Baer, J. Nunziato, A two-phase mixture theory for the deflagration-to-detonation transition (DDT) in reactive granular materials, International Journal of Multiphase Flow 12 (6) (1986) 861–889.

[17] F. Marble, Dynamics of a gas containing small solid particles, Combustion and Propulsion (5th AGARD Colloquium) (1963) 175–213.

[18] R. Abgrall, R. Saurel, Discrete equations for physical and numerical compressible multiphase mixtures, Journal of Computational Physics 186 (2) (2003) 361–396.

[19] E. Franquet, V. Perrier, Runge–Kutta discontinuous Galerkin method for the approximation of Baer and Nunziato type multiphase models, Journal of Computational Physics 231 (11) (2012) 4096–4141.

[20] E. Godlewski, P. Raviart, Numerical approximation of hyperbolic systems of conservation laws, Vol. 118, Springer Science & Business Media, 2013.

[21] R. Saurel, S. Le Martelot, R. Tosello, E. Lapébie, Symmetric model of compressible granular mixtures with permeable interfaces, Physics of Fluids 26 (12) (2014) 123304.

[22] A. Chinnayya, E. Daniel, R. Saurel, Modelling detonation waves in heterogeneous energetic materials, Journal of Computational Physics 196 (2) (2004) 490–538.

[23] D. Lhuillier, C. Chang, T. Theofanous, On the quest for a hyperbolic effective-field model of disperse flows, Journal of Fluid Mechanics 731 (2013) 184–194.

[24] T. McGrath, J. St. Clair, S. Balachandar, A compressible two-phase model for dispersed particle flows with application from dense to dilute regimes, Journal of Applied Physics 119 (17) (2016) 174903.

[25] R. Houim, E. Oran, A multiphase model for compressible granular-gaseous flows: formulation and initial tests, Journal of Fluid Mechanics 789 (2016) 166–220.

[26] Y. Zeldovich, Gravitational instability: An approximate theory for large density perturbations, Astronomy and astrophysics 5 (1970) 84–89.

[27] R. Saurel, E. Daniel, J. Loraud, Two-phase flows - Second-order schemes and boundary conditions, AIAA Journal 32 (6) (1994) 1214–1221.

[28] G. Rudinger, Some effects of finite particle volume on the dynamics of gas-particle mixtures, AIAA Journal 3 (7) (1965) 1217–1222.

[29] A. Kapila, R. Menikoff, J. Bdzil, S. Son, D. Stewart, Two-phase modeling of deflagration-to-detonation transition in granular materials: Reduced equations, Physics of Fluids 13 (10) (2001) 3002–3024.

[30] J. Bdzil, R. Menikoff, S. Son, A. Kapila, D. Stewart, Two-phase modeling of deflagration-to-detonation transition in granular materials: A critical examination of modeling issues, Physics of Fluids 11 (2) (1999) 378–402.

[31] J. Ghidaglia, A. Kumbaro, G. Le Coq, On the numerical solution to two fluid models via a cell centered finite volume method, European Journal of Mechanics-B/Fluids 20 (6) (2001) 841–867.

[32] Z. Naumann, L. Schiller, A drag coefficient correlation, Z Ver Deutsch Ing 77 (1935) 318–323.

[33] A. Chiapolino, R. Saurel, B. Nkonga, Sharpening diffuse interfaces with compressible fluids on unstructured meshes, Journal of Computational Physics 340 (2017) 389–417.

[34] D. Furfaro, R. Saurel, A simple HLLC-type Riemann solver for compressible non-equilibrium two-phase flows, Computers and Fluids 111 (2015) 159–178.

[35] O. Le Métayer, J. Massoni, R. Saurel, Elaborating equations of state of a liquid and its vapor for two-phase flow models; élaboration des lois d'état d'un liquide et de sa vapeur pour les modèles d'écoulements diphasiques, International Journal of Thermal Sciences 43 (3) (2004) 265–276.

[36] X. Rogue, G. Rodriguez, J. Haas, R. Saurel, Experimental and numerical investigation of the shock-induced fluidization of a particles bed, Shock Waves 8 (1) (1998) 29–45.

[37] M. Lallemand, R. Saurel, Pressure relaxation procedures for multiphase compressible flows, Tech. rep., INRIA Report (2000).

[38] P. Sweby, High resolution schemes using flux limiters for hyperbolic conservation laws, SIAM Journal on Numerical Analysis 21 (5) (1984) 995–1011.

[39] J. Brackbill, D. Kothe, C. Zemach, A continuum method for modeling surface tension, Journal of Computational Physics 100 (2) (1992) 335–354.

[40] G. Perigaud, R. Saurel, A compressible flow model with capillary effects, Journal of Computational Physics 209 (1) (2005) 139–178.

[41] A. Chauvin, Etude expérimentale de l'atténuation d'une onde de choc par un nuage de gouttes et validation numérique, Ph.D. thesis, Aix-Marseille University (2012).

480